

3D morphological analysis of local elastic fields in a cementitious material

Julie Escoda, François Willot, Dominique Jeulin, Julien Sanahuja, Charles Toulemonde

▶ **To cite this version:**

Julie Escoda, François Willot, Dominique Jeulin, Julien Sanahuja, Charles Toulemonde. 3D morphological analysis of local elastic fields in a cementitious material. Advances in Structural. Engineering and Mechanics (ASEM11), 2011, Seoul, South Korea. hal-00879268

HAL Id: hal-00879268

https://minesparis-psl.hal.science/hal-00879268

Submitted on 2 Nov 2013

HAL is a multi-disciplinary open access archive for the deposit and dissemination of scientific research documents, whether they are published or not. The documents may come from teaching and research institutions in France or abroad, or from public or private research centers.

L'archive ouverte pluridisciplinaire **HAL**, est destinée au dépôt et à la diffusion de documents scientifiques de niveau recherche, publiés ou non, émanant des établissements d'enseignement et de recherche français ou étrangers, des laboratoires publics ou privés.

3D morphological analysis of local elastic fields in a cementitious material

*J. Escoda[1)2)], F.Willot[1)], D. Jeulin[1)], J. Sanahuja[2)], C. Toulemonde[2)]

[1)] *Centre de Morphologie Mathématique, Mathématiques et Systèmes, Mines ParisTech, Fontainebleau, France*
[2)] *Département Matériaux et Mécanique des Composants, EDF R&D, Moret-sur-Loing, France*
julie.escoda@ensmp.fr

ABSTRACT

The linear elastic fields occurring in a cementitious material are numerically computed and analyzed in order to determine the spatial arrangement between the microstructure and high-stress regions in the matrix. The microstructure is obtained by segmentation of a mortar sample microtomography whereas fields are evaluated on the 3D image grid using the FFT algorithm for both hydrostatic and shear strain loading. Different contrasts, i.e. ratios of the Young moduli between aggregates and matrix are considered: 10^{-8}, 3, 100, 1000 and 10^{4}. Various components of the stress tensor are successively analyzed, corresponding to the component "parallel" to the applied loading and invariant components. Regions of stress concentration are correlated to the skeleton by influence zone of the aggregates phase. Moreover, when hydrostatic strain loading is applied, the highest values of the von Mises component of the stress tensor are both on the aggregates skeleton and at low distance from aggregates.

Similar analysis of the local fields are carried out on a simulated microstructure made of boolean random polyhedra and compared with results on the real mortar microstructure.

1. INTRODUCTION

The purpose of this work is to study the effect of the microstructure on the mechanical properties of mortar composites, and in particular, on the local elastic response. The microstructure of mortar and other cementitious media is complex ; among others, it results from a usually dense arrangement of gravels in space, and of a certain granulometry, i.e. a multi-scale distribution of sizes and shapes for the grains. Additionally, such materials often contain both micro and macro pores. In situation of low contrast of properties between the grains and matrix, and at low porosity, the effective (i.e. macroscopic) linear elastic response depends on the grains and pores volume fraction ; to investigate more physically relevant behavior, typically viscoelasticity, a detailed description of the microstructure is required.

Numerous attempts to study numerically concrete materials have been made. (Nagai 1998) used a 3D concrete microstructure reconstructed from 2D successive sections to investigate both linear elastic behavior and cracks along the interface between aggregates and matrix. Microtomography has been used by (Hain 2007) to study linear elastic and viscoplastic behavior of hardened cement paste by the finite element method (FEM). Various random models of cementitious materials have been developed as well. For mortar and cement material, the model of (Bentz 1997) which takes into account hydration process, has been used by (Hain 2007; Haecker 2005; Bernard 2008) to investigate linear elasticity of cement paste and of mortar. (Smilauer 2010) also used Bentz model combined with Fast-Fourier Transform method to study viscoelastic behavior of cement paste. They considered random microstructures of various sizes, the largest containing 200x200x200 voxels, and low Young modulus contrast between matrix and aggregates. (Bary 2009) modeled cement paste as inclusions and pores embedded in the C-S-H matrix.

The purpose of this work is two-fold : to investigate not only the effective properties of mortar composites, but also the local elastic response in a mortar sample, and link it with geometrical parameters computed from the microstructure. To this aim, a 3D gray-level microtomography image is segmented into three phases : voids, gravels and cement (matrix). The elastic fields are readily computed using the numerical "FFT method", which is directly applied to the segmented microstructure. The cement/matrix contrast of properties is used to monitor different behavior for the composites: small in cases of strongly damaged media, close to 1 for real mortar samples, and large to anticipate the needs for viscoelastic computations (Sanahuja 2011). To study the spatial correlation between the microstructure and regions of stress concentration, two methods are used: the first method evaluates the mean of a given component of the stress field in the matrix as a function to the distance to a set (for example aggregates or voids phase); the second method evaluates preferential association between two sets (one region of the matrix corresponding to a range of values of the considered component of the stress tensor and one set derived from the microstructure).

In the second part of this work, a basic microstructure model is proposed to account for the microstructure granulometry. It is emphasized that the model is one-scale, but could easily be generalized to multi-scale materials. Such model allows for the systematic study of microstructure/properties relation. Some of these results are presented here.

2. EFFECTIVE AND LOCAL ELASTIC RESPONSE

In the following, the elastic response of two types of microstructures are considered: a real mortar microstructure in section 4 and a Poisson polyhedra Boolean random model in section 5.

The local linear elastic response in the matrix and aggregates is defined by means of the local linear elastic tensor L, which relates the second order strain and stress tensor fields σ and ε by:

$$\sigma_{ij} = L_{ij,kl}\varepsilon_{kl}, \tag{1}$$

where the stress (resp. strain) field satisfies the equilibrium (resp. admissibility) condition, i.e.:

$$\partial_i \sigma_{ij} = 0, \quad \varepsilon_{kl} = 1/2(\partial_k u_l + \partial_l u_k). \tag{2}$$

In the above, the local displacement field is noted u_k, and small deformation is assumed. It is assumed that each phase of the microstructure is isotropic, so that the local elastic tensor L is determined by its Poisson ratio and Young's modulus. Note that, in the voids, $L \equiv 0$, i.e. the stress is zero and the strain is finite.

As measured by (Granger 1996), the Poisson ratio is taken as a phase-independent constant equal to 0.2 (matrix and aggregates phases). As a result, the problem only depends on the Young's moduli aggregate-matrix contrast, defined as $\chi \equiv E^{(a)} / E^{(m)}$. Values of contrast χ equal to 10^{-8}, 3, 100, 1000 and 10^4 are successively considered. The value $\chi \equiv 3$ is close to that found in real mortar samples.

The material is subjected to hydrostatic as well as shear strain loading, defined respectively as:

$$\left\langle \varepsilon_{ij} \right\rangle = \varepsilon_0 \delta_{ij}, \quad \left\langle \varepsilon_{ij} \right\rangle = \begin{cases} \varepsilon_0 \text{ if ij} = \text{xy or ij} = \text{yx}, \\ 0 \text{ otherwise}, \end{cases} \tag{3}$$

where ε_0 is a scalar.

Full-field computations are undertaken using the "augmented Lagrangian" algorithm (Michel 2001), one of the Fast Fourier Transform that is especially efficient for handling infinitely-contrasted media. The algorithm is best understood in its original form, derived by (Moulinec 1994). Referring to the Lippmann–Schwinger equations (Eqs. (4) and (5)) :

$$\varepsilon_{ij}(\mathbf{x}) = \left\langle \varepsilon_{ij} \right\rangle - \int \mathrm{d}^3 \mathbf{x}' G^{(0)}_{ij,kl}(\mathbf{x} - \mathbf{x}') \tau_{kl}(\mathbf{x}'), \tag{4}$$

$$\tau_{ij}(\mathbf{x}) \equiv \sigma_{ij}(\mathbf{x}) - L^{(0)}_{ij,kl} : \varepsilon_{kl}(\mathbf{x}), \tag{5}$$

where $L^{(0)}$ is a given "reference" elastic tensor that is homogeneous and $G^{(0)}$ is its associated Green's function. Eq. (4) is computed in the Fourier domain while Eq. (5) is computed in the real space, with Fast Fourier transforms used to iterate between the two. The authors refer to (Michel 2001) for details of the augmented Lagrangian scheme, not given here. Among the main advantages of the method, the FFT algorithms do not require meshing of the microstructure images, hence it handles arbitrarily complex images. Second, numerical experiments show that large-size systems are efficiently handled by this algorithm, in terms of speed and memory, including for highly-contrasted composites.

3. MORPHOLOGICAL TOOLS FOR MEASURING SPATIAL SET CORRELATIONS

To determine quantitatively spatial correlation between one of the material phases (i.e. aggregates or voids) and regions of stress concentration, two methods are considered. Both involve the use of the dilation operation (Serra 1982) of a set A by a structuring element (of increasing size r) $B(r)$ defined as $A \oplus B(r) = \left\{ \cup B_{\mathbf{x}}(r), \mathbf{x} \in A \right\}$, with $B_{\mathbf{x}}(r)$ the translation of $B(r)$

by **x**. The structuring element *B(r)* used for dilations is a rhombicuboctahedron of radius *r*, to numerically approximate a ball (see Fig. 1).

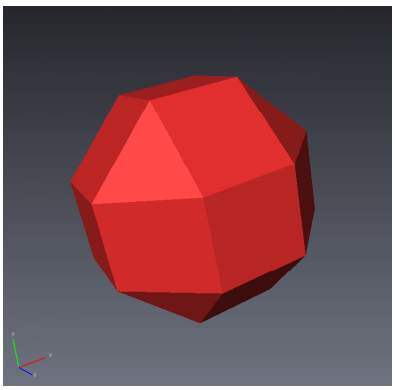


Fig. 1. 3D view of a rhombicuboctahedron

The first method consists in evaluating the mean $m_j(r)$ of the stress field in the matrix as a function of the distance *r* to a given set A_j. Equivalently, $m_j(r)$ is the average of the field on the region

$$X_r = \left(A_j \oplus B(r)\right) \cap \left(A_j \oplus B(r-1)\right)^c \cap A_m, \tag{6}$$

where c denotes the complementary set, and A_m is the matrix phase. A 2D slice of an example of the sets used in this method is given in Fig. 2.

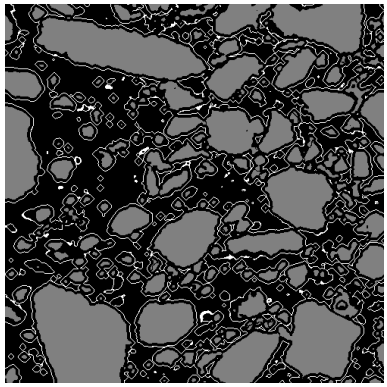


Fig. 2. 2D section of sets used to evaluate the mean $m_a(r)$ of a field in the matrix at a distance r = 5 voxels of aggregates. Aggregates are given in gray and the set X_r is given in white.

The second morphological tool, based on the "increasing neighborhoods method", is used to measure the spatial "arrangement" between two sets (Jeulin 1986). This method evaluates, for increasing values of *r*, the function ρ_j which is defined as

$$\rho_j(r) = \frac{\Phi_j(r)}{P\{\mathbf{x} \in (A_k \oplus B(r))\} - p_k} \frac{1 - p_k}{p_j},$$
$$\Phi_j(r) = P\{\mathbf{x} \in (A_k \oplus B(r)) \cap A_j\}, \tag{7}$$

where p_j (resp. p_k) is the volume fraction of the phase A_j (resp. A_k). A 2D slice of an example of the sets used in this method is given in Fig. 3. The function ρ_j depends on the two functions F and F_j, the distribution of distances of a random point $\mathbf{x}$ in A_k^c to the boundary of A_k, and the distribution of distances of a random point $\mathbf{x}$ in A_j to the boundary of A_k respectively:

$$F(r) = P\{d(\mathbf{x}, A_k) < r, \mathbf{x} \in A_k^c\} = \frac{P\{\mathbf{x} \in (A_k \oplus B(r))\} - p_k}{1 - p_k},$$
$$F_j(r) = P\{d(\mathbf{x}, A_k) < r, \mathbf{x} \in A_j\} = \frac{\Phi_j(r)}{p_j}, \tag{8}$$
$$\rho_j(r) = \frac{F_j(r)}{F(r)},$$

The interpretation of the function $\rho_j(r)$ is as follow: at the scale r, there is a preferential association (resp. a repulsion effect) between sets A_k and A_j when $\rho_j(r)>1$ (resp. $\rho_j(r)<1$). Hereafter, the increasing neighborhoods method is applied to one of the material phases and to a set obtained by the thresholding of one of the stress field component in the matrix (resp. A_j and A_k in the equations above).

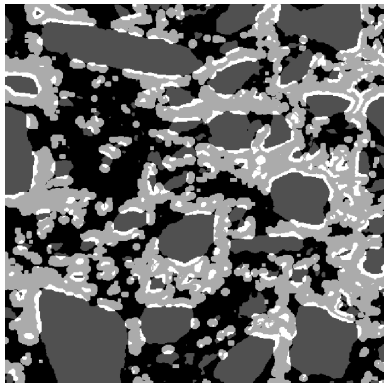
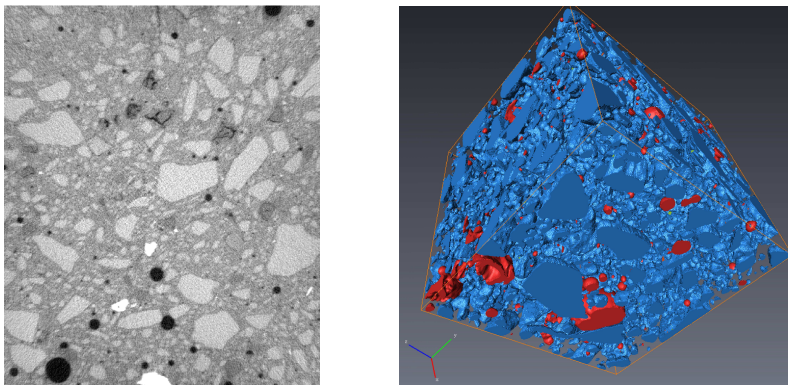


Fig. 3. 2D section of the sets used to evaluate the function $\rho_j(r)$ at r= 5 voxels. Aggregate phase (set A_j) is given in dark gray, $A_k \oplus B(r)$ (A_k corresponds to a range of values of the considered stress field component) is given in light gray and their intersection is given in white.

4. LOCAL ELASTIC RESPONSE OF A MORTAR MICROSTRUCTURE

In this section, a real mortar material microstructure is considered. It was obtained by segmentation of a 3D microtomography image of mortar (Escoda 2011) into three phases: aggregates, voids and matrix (cement paste). A 2D cut of the microtomography image as well as a 3D view of the mortar microstructure are given in Fig. 4. Two-dimensional cuts of the field maps, obtained using the FFT algorithm, are given, for both hydrostatic strain loading and shear strain loading in (Fig. 5 and Fig. 6 resp.).



(a) (b)

Fig. 4. 2D section of a 3D mortar image obtained by microtomography (a) and 3D view of the corresponding mortar microstructure (b). The mortar microstructure results from the segmentation of the gray-level image (a) into three phases: matrix, aggregates and voids. In the microstructure (b), aggregates are represented in blue, voids in red, and the matrix is transparent.

4.1. Component of the stress field "parallel" to the applied loading

Evaluation of the function $m_j(r)$ for various sets A_j In the following, the function $m_j(r)$ is computed for the component of the stress field parallel to the applied loading, i.e. σ_m or σ_{xy} when hydrostatic or shear strain loading is applied, respectively. Sets A_j made of aggregates, voids or the skeleton by influence zone (SKIZ), as defined by (Lantuejoul 1980), of the aggregates, are considered first (see Fig. 7 for a representation of the SKIZ). In order to obtain a more accurate determination of the localization of high stress field regions, a subset of the SKIZ aggregates is also considered.

Graphs of the functions $m_a(r)$ and $m_s(r)$ (mean at the distance r to the aggregates phase and to the SKIZ respectively, in the matrix) are shown in Fig. 8 for various contrasts and with either hydrostatic or shear strain loading. The SKIZ is determined in 3D by taking the watershed of the distance function to the aggregates (Fig. 7). Contrary to the aggregate set, regions far from the aggregates correspond to small values of r.

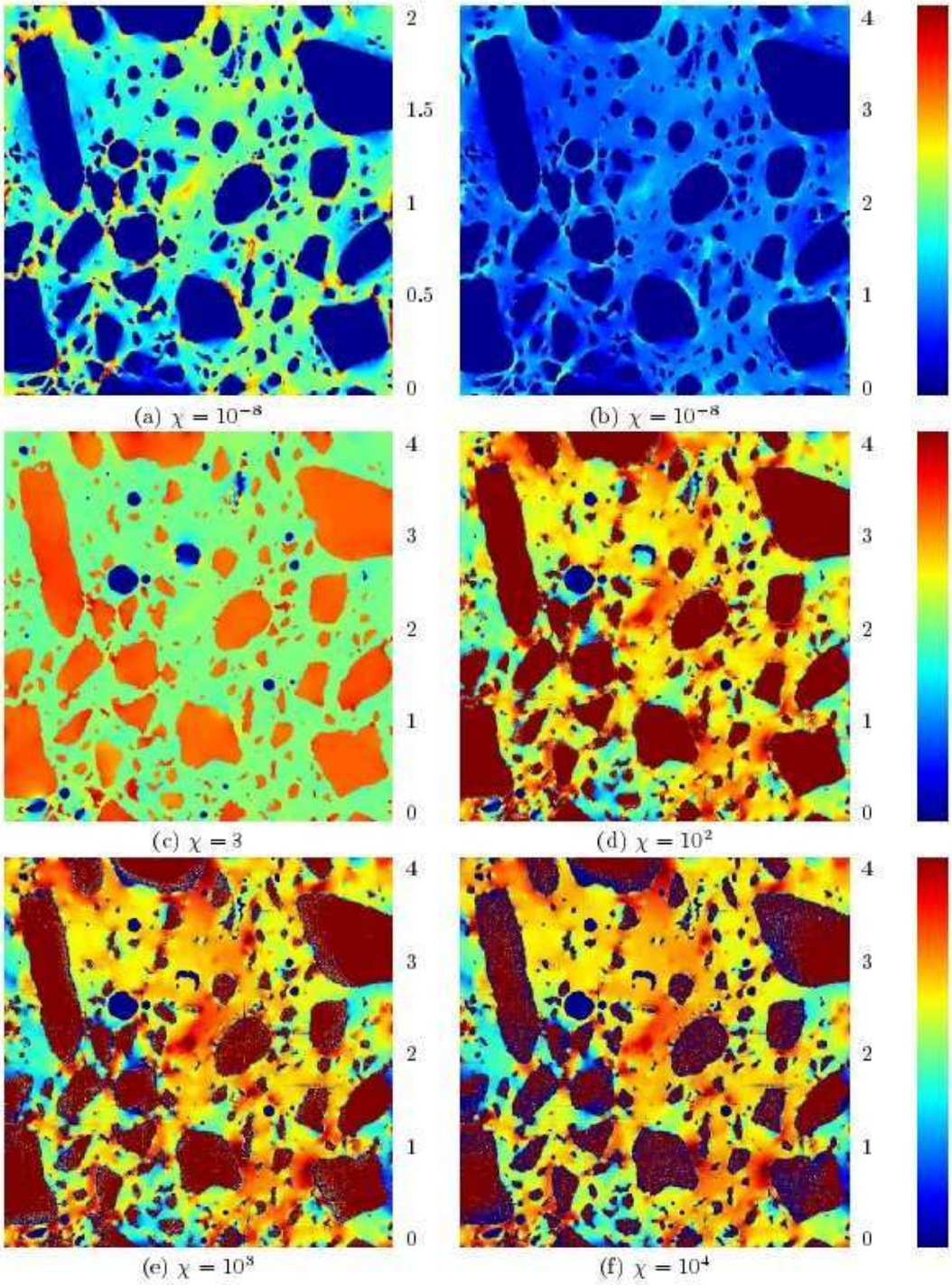


Fig. 5. 2D sections of the normalized stress component $\sigma_m/[E^{(m)}<\varepsilon_m>]$ at varying contrasts $\chi=E^{(a)}/E^{(m)}$. To emphasize the field patterns, the maps are thresholded according to the color-scale as shown on the right. Hydrostatic strain loading is applied with $<\varepsilon_m>= \varepsilon_0$.

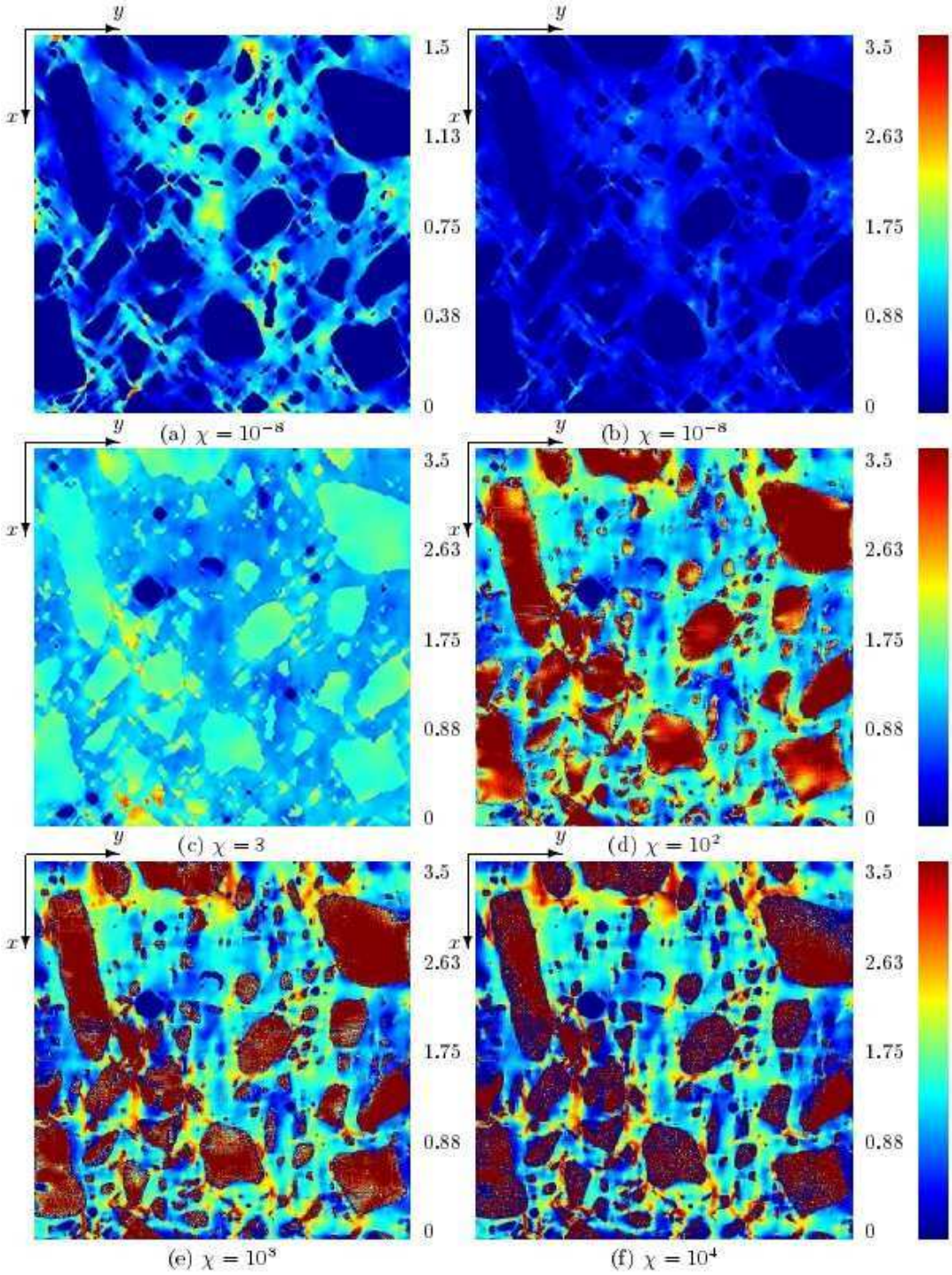


Fig. 6. 2D sections of the normalized stress component $\sigma_{xy}/[E^{(m)}<\varepsilon_{xy}>]$ at varying contrasts $\chi=E^{(a)}/E^{(m)}$. The field maps are thresholded according to the color-scale as shown right. Shear strain loading is applied with $<\varepsilon_{xy}>=\varepsilon_0$.

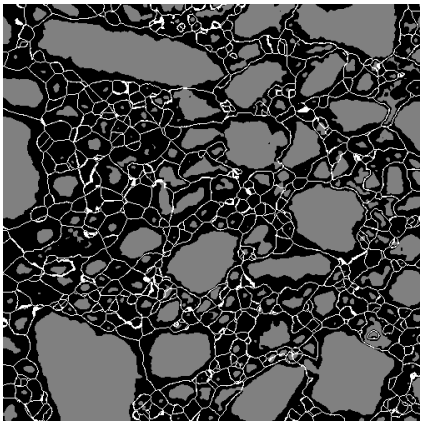


Fig. 7. 2D section of the skeleton by influence zone (SKIZ) of the aggregates phase. Aggregates are given in gray and the SKIZ is given in white.

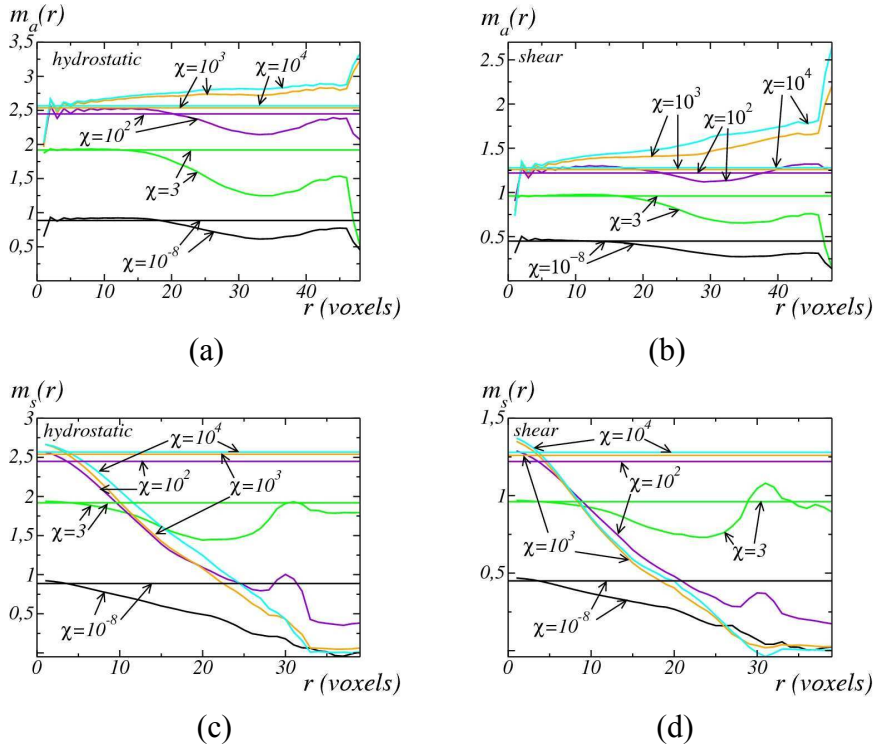


Fig. 8. Mean $m_{a,s}(r)$ of the parallel stress component σ_m or σ_{xy} as a function of the distance r at various aggregates/matrix contrasts χ. The distance r is computed from the aggregates (a, b) or from the aggregates SKIZ (c, d). Hydrostatic or shear strain loading is applied (a, c and b, d, resp.). A straight horizontal line indicates the mean stress component in the matrix, associated to each contrast value.

At large contrasts, it appears that the parallel stress field is statistically highest at large distances r of the aggregates. Indeed, when $\chi=10^4$ or $\chi=10^3$, independently of the loading

direction, $m_a(r)$ increases with r (Figs. 8(a) and 8(b)), whereas the inverse trend is observed for $m_s(r)$ (Figs. 8(c) and 8(d)), i.e. when the distance is measured from the aggregates SKIZ. Equivalently, the region of the matrix near the aggregates SKIZ is subjected to strain and stress fields that are higher than the average applied field. These two results indicate that high-stress regions are to be found far away from the aggregates. Such effect is in agreement with visual observation of the maps (Fig. 9), where the stress field together with the aggregates SKIZ superimposed in blue, are shown.

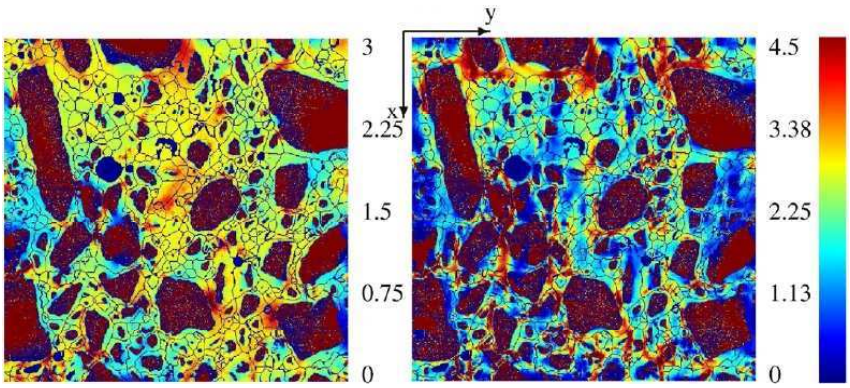
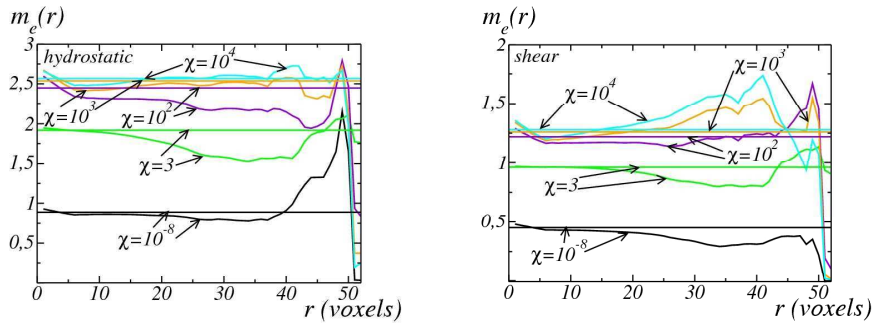


Fig. 9. 2D cut at $z=cst$ of the parallel stress component σ_m and σ_{xy} (maps a and b, resp.) with applied hydrostatic or shear strain loading, resp., with aggregates/matrix contrast $\chi=10^4$. The stress field values correspond to the color scale at right (values outside of the range given at the right of each map are thresholded). The aggregates SKIZ is superimposed on the maps and shown in blue. The 3D image is of size 2.5 × 3 × 2.5 cm^3 and of resolution 25 µm/voxel.

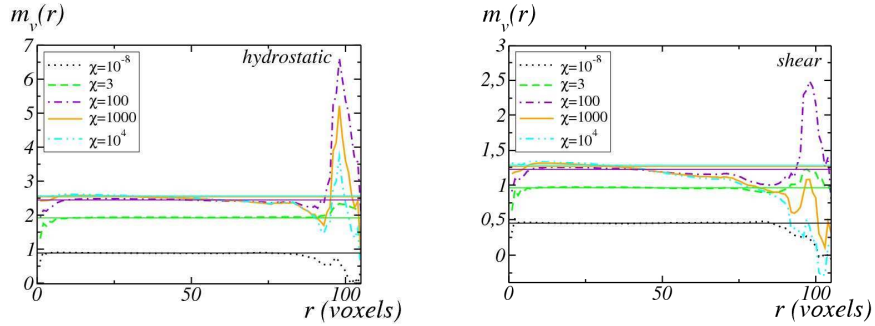
In order to study more accurately the location of zones of the matrix with high values of the parallel component of the stress field, a subset of the SKIZ is used as follow. Indeed it appears in Fig. 9 that regions of stress concentration are located around some specific parts of the SKIZ. As such, it is useful to investigate whether the location of high-stress zones is linked with the distance between adjacent aggregates. More precisely, it is unclear whether these regions correspond to regions between aggregates close to each other, or equivalently to parts of the SKIZ located at low distance from the aggregates. To this aim, the extinction function is used: this function is defined on the SKIZ and is equal to the distance function to the aggregates phase. The extinction function is thresholded between 0 and 7 voxels (the latter value being visually determined): the result of this thresholding is the subset A_e of the aggregates SKIZ containing points at a distance lower than 7 voxels. The function $m_e(r)$ is then evaluated for $A_j=A_e$. The resulting graph of $m_e(r)$ is given in Fig. 10 for both hydrostatic and shear strain loading. Accordingly, there is no preferential association between regions of stress concentration and regions between aggregates close to one another. Indeed, with the hypothesis of such association, $m_e(r)$ would have been significantly higher than $m_s(r)$ at low values of r, whereas in the obtained results, the difference between $m_e(1)$ and $m_s(1)$ is about 1% for each contrast and loading type.



(a) (b)

Fig. 10. Mean $m_e(r)$ of the parallel stress component σ_m or σ_{xy} as a function of the distance r to thresholded extinction function (between 0 and 7), at various aggregates/matrix contrasts χ. Hydrostatic or shear strain loading is applied (a and b resp.). At each contrast, a straight horizontal line indicates the mean stress component in the matrix.

In order to evaluate the influence of voids phase on stress concentration zones spatial repartition, graphs of the mean of the parallel stress field component in the matrix at a distance r of the voids $m_v(r)$ are given in Fig. 11. There is no preferential association between voids and regions of high values of stress component parallel to the applied loading. Indeed, for $r>80$ voxels, volumes on which the mean m_v is evaluated are too small too obtain relevant values of $m_v(r)$ and only the first part of the graph ($r<80$) is relevant.



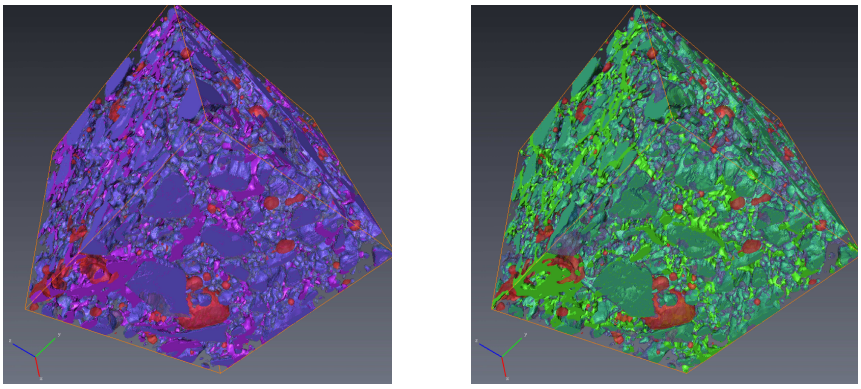
(a) (b)

Fig. 11. Mean $m_v(r)$ of the parallel stress component σ_m or σ_{xy} as a function of the distance r to voids, at various aggregates/matrix contrasts χ. Hydrostatic or shear strain loading is applied (a and b resp.). At each contrast, a straight horizontal line indicates the mean stress component in the matrix.

Increasing neighborhoods method In this section, the increasing neighborhoods method is used to determine the spatial correlation between some regions of the matrix containing specific values of the parallel stress field component and the microstructure. To this aim, the field is thresholded, to study successively regions containing high values and values closed to 0. The

function $\rho_j(r)$ is evaluated by taking the aggregates phase or the voids as the set A_j , and noted $\rho_a(r)$ and $\rho_v(r)$, resp.

First, for each loading mode, A_k is the region of the matrix where the parallel stress component is higher than a chosen threshold. This threshold is so that the volume of A_k equals 5% of the matrix volume. Since this second method is based on the dilation of the set A_k (see Eq. 6)), low values of r correspond to regions subjected to high stress. A 3D map of the thresholded stress field is shown in purple and green in Fig. 12.



(a) (b)

Fig. 12. 3D view of the microstructure (aggregates in blue, voids in red and transparent matrix), and of the thresholded stress field component σ_m (resp. σ_{xy}) when hydrostatic (resp. shear) strain loading is applied, in purple (a) and green (b) respectively. The matrix/aggregates contrast $\chi=10^4$ is fixed.

The resulting functions $\rho_a(r)$ and $\rho_v(r)$ are plotted as functions of the distance r at various contrasts χ, with hydrostatic and shear strain loading conditions in Fig. 13. Consistently with the results obtained using the mean stress functions $m_{a,s}(r)$, regions of high stress are not located close to grains. The grains concentration is indeed significantly lower than 1 when r is small, i.e. in regions subjected to high stress, independently of the loading direction (Figs. 13(a) and 13(b)). Additionally, at high contrasts, high stress regions are not located around voids. Indeed, as shown in Figs. 13(c) and 13(d), the function $\rho_v(r)$ is always smaller than 1, except at low-contrast and when the grains behave as voids ($\chi=3$ and $\chi=10^{-8}$, resp.). At low aggregates/matrix contrast, indeed, the effect of aggregates is negligible and the elastic response is analogous to that of a matrix with isolated voids, around which stress is concentrated.

The histogram of the stress component parallel to the applied loading in the matrix (see Fig. 14) contains a shouldering when the value of the field goes through 0, similar to a jump at 0. To investigate the regions responsible for this behavior, the increasing neighborhoods method is used, for a contrast $\chi=10^4$, with the regions $A_k = \{\mathbf{x}, |\sigma_m(\mathbf{x})| \leq 1.5\}$ and $A_k = \{\mathbf{x}, |\sigma_{xy}(\mathbf{x})| \leq 2\}$ in the case of hydrostatic and shear strain loading respectively, whereas the set A_j is successively equal to the aggregates phase and voids phase (see Fig. 15). These two sets are used to determine the spatial arrangement between the “shouldering” regions and these two phases. These graphs

indicate that the regions corresponding to the shouldering in the histograms are located at a low distance from aggregates.

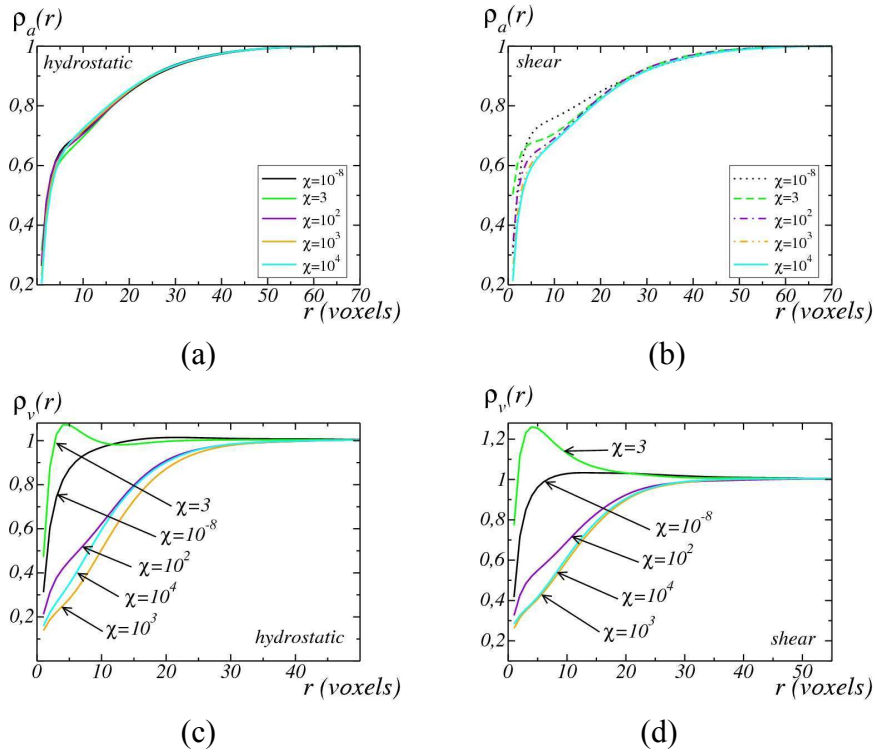


Fig. 13. Function $\rho_{a,v}(r)$ used to measure the correlation between one of the material phase (a, b: aggregates, c, d: voids) and regions of high-stress. Hydrostatic or shear strain loading is applied (a, c and b, d, resp.). High-stress regions are determined by a thresholding of the parallel stress component σ_m or σ_{xy}.

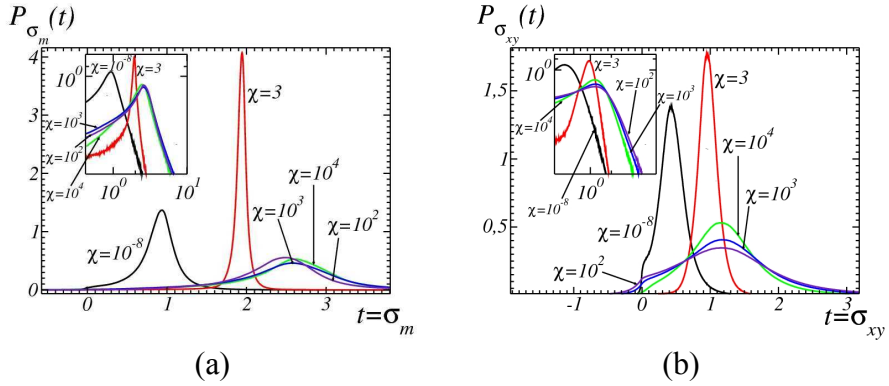
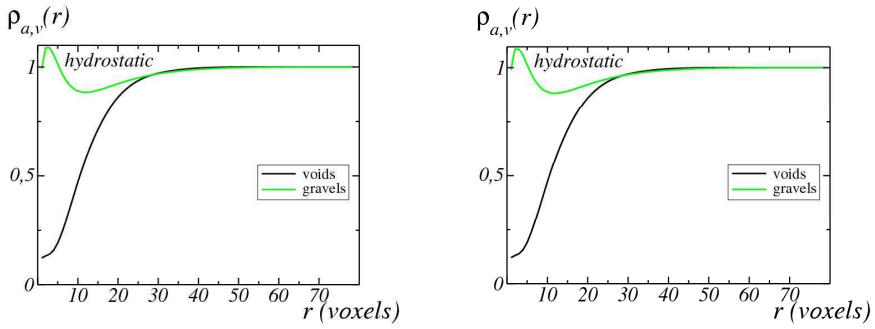


Fig. 14. Field histograms $P\sigma_m(t)$ and $P\sigma_{xy}(t)$, i.e. probability density values, of the mean stress field σ_m and of the shear stress component σ_{xy} (a and b resp.), at varying contrasts $\chi=E^{(a)}/E^{(m)}=10^{-8}$, 3, 100, 1000, 10^4. Inserted graphs: behavior of the distribution at high stress values (t large) in log-log scale.



(a) (b)

Fig. 15. Function $\rho_{a,v}(r)$ used to measure the correlation between one of the material phase (aggregates and voids) and regions corresponding to the shouldering in the histogram (in the matrix) of σ_m and σ_{xy}, when hydrostatic or shear strain loading is applied (a and b resp.). The contrast $\chi=10^4$ is considered in this analysis.

4.2. Local analysis of the invariant components

In this section, three other components of the stress field are considered: the von Mises component σ_{eq} defined as

$$\sigma_{eq}^2 = 3/2\sigma_{ij}\sigma_{ij} - 1/2\sigma_{ii}^2, \tag{9}$$

where repeated indices are summed; the highest principal stresses (i.e. the highest eigenvalues of the stress tensor), and its trace

$$\sigma_m = 1/3\sigma_{ii}. \tag{10}$$

For each of these components, and for both hydrostatic and shear strain loadings, graphs of the mean $m_a(r)$ and $m_s(r)$ of the field in the matrix phase at distance r from aggregates and from their SKIZ respectively are given.

In Fig. 16, functions $m_{a,s}(r)$ are computed for the von Mises component. As for the study of the parallel stress component, a concentration of the von Mises component occurs around the aggregates SKIZ, for both hydrostatic and shear strain loadings. In the case of hydrostatic strain loading, the graph also indicates a concentration of high values of the von Mises component at small distance of the aggregates phase (Fig. 16(a)).

Finally, the functions $m_{a,s}(r)$ are evaluated for the trace of the stress tensor σ_m (see Fig. 17). In the case of an hydrostatic strain loading, the results were already given in the section 4.1 (Figs. 8(a) and 8(c)). For the shear strain loading case, the graph 17(a) indicates there is local traction at medium distance of the aggregates (distance between 5 and 20 voxels).

The functions $m_{a,s}(r)$ evaluated for the highest principal value (see Fig. 18) gives similar results to the functions $m_{a,s}(r)$ evaluated for the parallel stress component and leads to the same

conclusion of a stress concentration on the aggregates SKIZ: high-stress regions of the principal stress values are located preferentially close to the SKIZ.

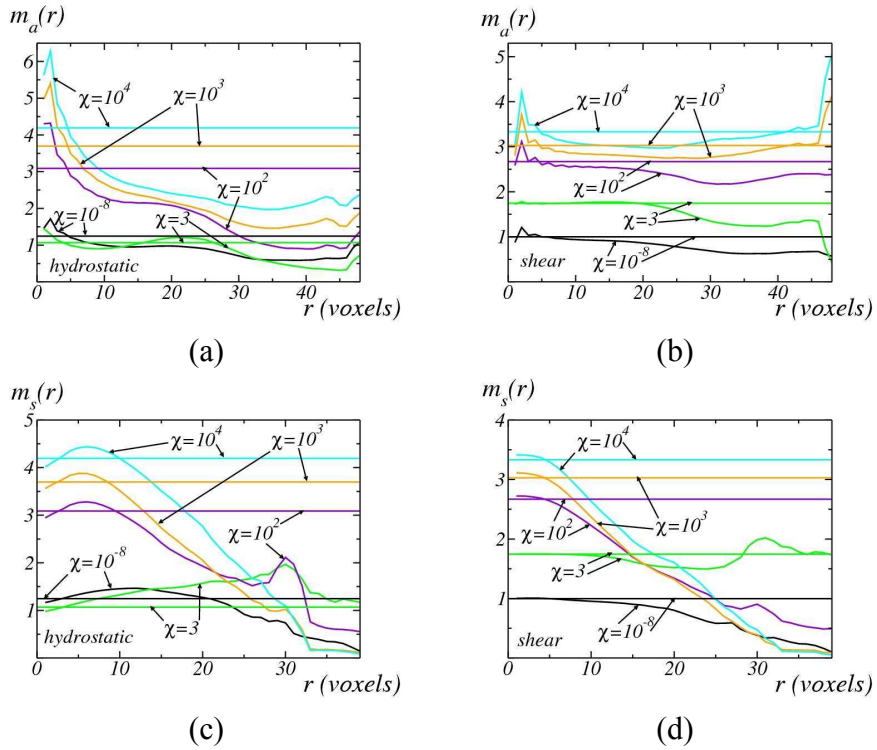


Fig. 16. Mean $m_{a,s}(r)$ of the von Mises component σ_{eq} as a function of the distance r at various aggregates/matrix contrasts χ. The distance r is calculated from the aggregates (a, b) or from the aggregates SKIZ (c, d). Hydrostatic or shear strain loading is applied (a, c and b, d, resp.). At each contrast, a straight horizontal line indicates the mean stress component in the matrix.

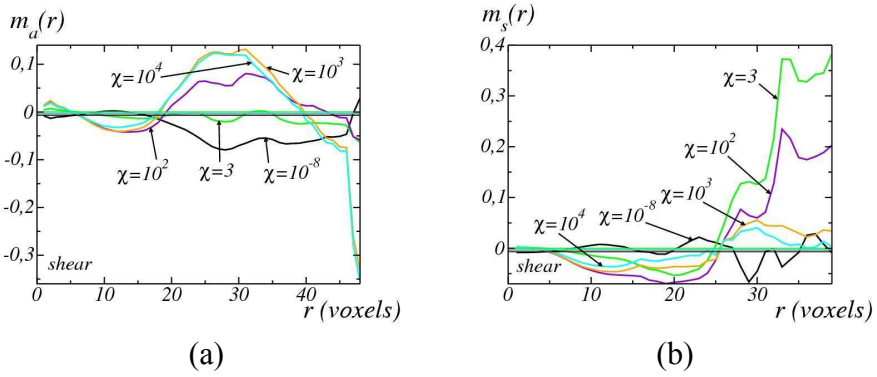


Fig. 17. Mean $m_{a,s}(r)$ of the trace σ_m of the stress tensor as a function of the distance r at various aggregates/matrix contrasts χ. The distance r is calculated from the aggregates (a) and from the aggregates SKIZ (b). Shear strain loading is applied. At each contrast, a straight horizontal line indicates the mean stress component in the matrix.

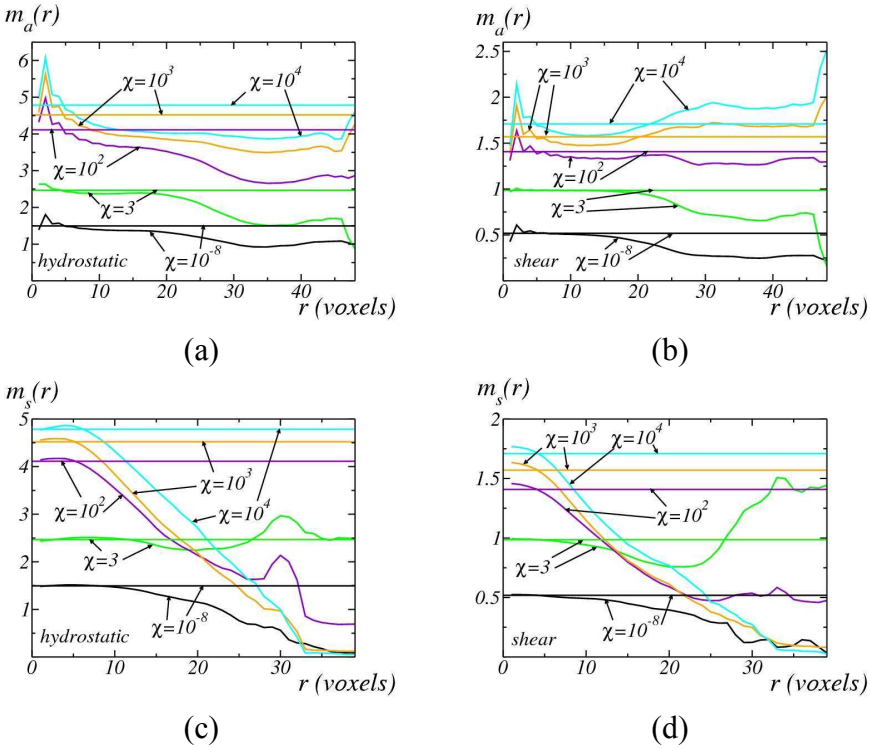


Fig. 18. Mean $m_{a,s}(r)$ of highest principal value of the stress tensor as a function of the distance r at various aggregates/matrix contrasts χ. The distance r is calculated from the aggregates (a, b) or from the aggregates SKIZ (c, d). Hydrostatic or shear strain loading is applied (a, c and b, d, resp.). At each contrast, a straight horizontal line indicates the mean stress component in the matrix.

5. RANDOM MICROSTRUCTURE MODELS FOR MORTAR COMPOSITES

5.1. Boolean polyhedra random model

In this section, mortar models are proposed where gravels are approximated by polyhedra. Realizations of 3D random Poisson polyhedra Boolean models are considered (Quenec'h 1992). Each realization consists of a set of interpenetrating Poisson polyhedra, located on Poisson points. Hence, the number of points in the image follows the Poisson distribution:

$$P\{n=k\}=e^{-N}\frac{N^k}{k!}, \tag{11}$$

where N is the expectation of the distribution. In our model, Poisson points are distributed uniformly in the image.

A Poisson polyhedron is generated from a Poisson tesselation of the image (implantation of Poisson plane of density λ). Poisson polyhedra are defined as the complementary set of this tesselation. For each polyhedra implantation on the Boolean model, a Poisson tesselation is generated and one Poisson polyhedron is randomly selected (i.e. a selection by number is undertaken, not by volume).

Accordingly to the classical relation for Boolean models, the polyhedra volume fraction p and the Poisson points density θ are linked by:

$$p = 1 - \exp(-\frac{6}{\pi^4 \lambda^3}\theta). \tag{12}$$

A Boolean random model of size 500^3 is generated (see Fig. 19). In this preliminary study, the parameters p=10.1% and λ=0.045 are chosen in order to obtain an aggregates phase which does not percolate and to get a representative volume.

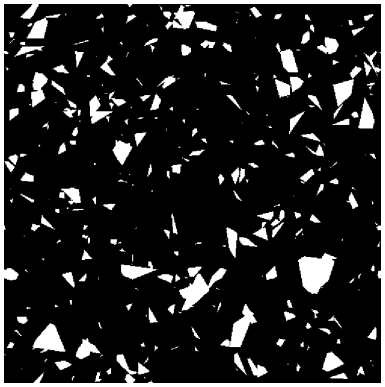


Fig. 19. 2D slice of a 3D Boolean Poisson polyhedra realization

5.2. Local fields analysis

Local elastic fields are computed on this microstructure using the FFT method for both hydrostatic and shear strain loading and for each contrast χ=10^{-8}, 3, 100, 1000 and 10^4 (see Figs. 20 and 21 for the map fields of the "parallel" stress component).

The mean of the "parallel" stress component is computed as a function of the distance to the aggregates and to their SKIZ (see Figs. 20(f) and 21(f) for a representation of this SKIZ superimposed to the map fields) for the two loadings modes, and for each contrast (see Fig. 22). As for the mortar microstructure, this computation shows that highest values of the "parallel" stress component are concentrated on the aggregate SKIZ.

CONCLUSION

Numerical elastic fields on a mortar sample for both hydrostatic and shear strain loadings have been analyzed in order to determine the preferential association between highest values of various components of the field and the material microstructure. Two methods were used: the first one evaluates the mean of the stress field as a function of the distance to a given set, whereas the second methods evaluates preferential associations between a set and a given range of the stress field. Regarding the "parallel" (with respect to the macroscopic strain loading) stress component, a first approximation of candidates zones of high-stress regions have been found, namely on the aggregates SKIZ, i.e. midway between aggregates. This result holds

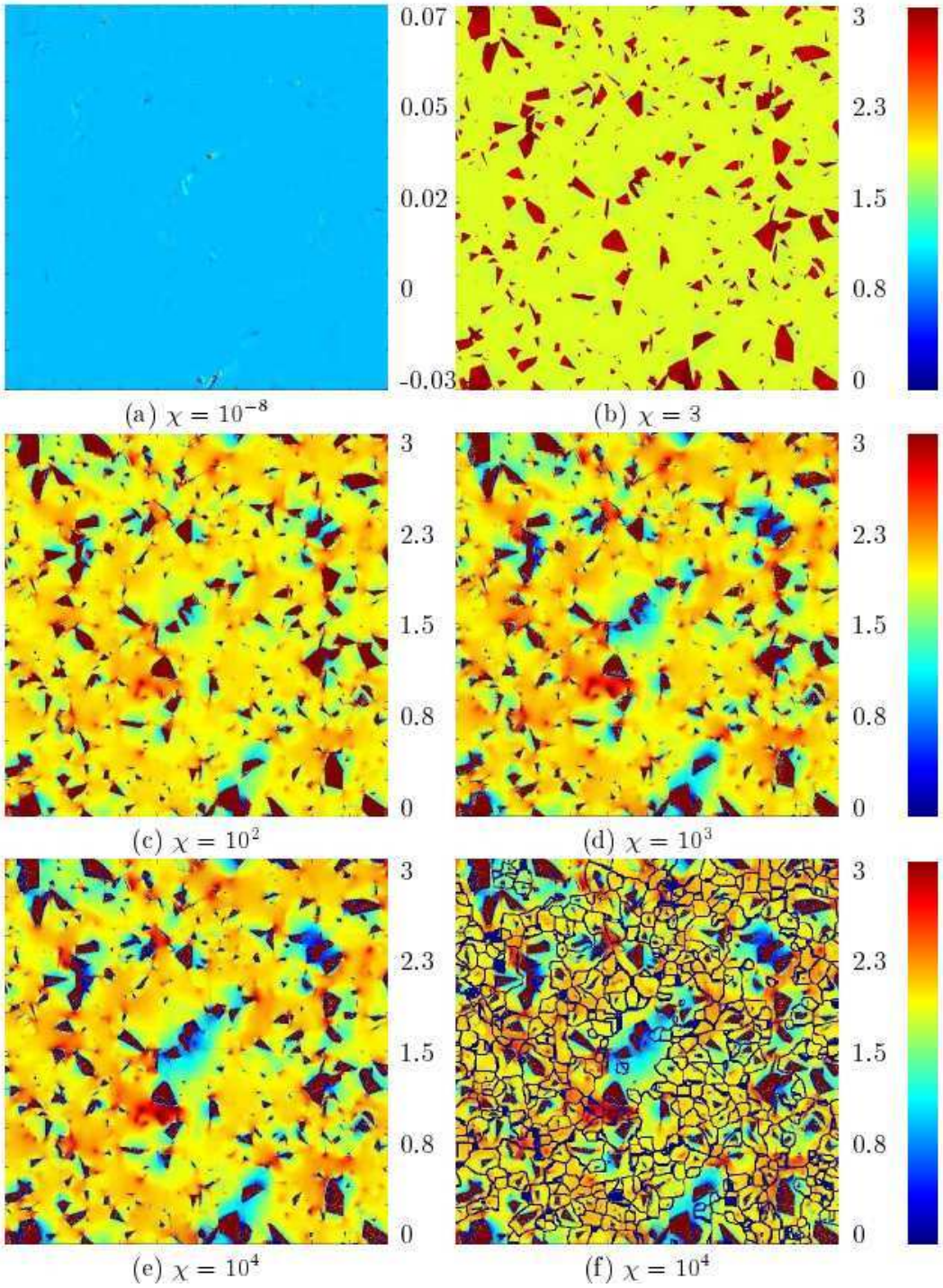


Fig. 20. 2D sections of the normalized stress component $\sigma_m/[E^{(m)}<\varepsilon_m>]$ at varying contrasts $\chi=E^{(a)}/E^{(m)}$. The field maps are thresholded according to the color-scale as shown right. Hydrostatic strain loading is applied with $<\varepsilon_{xy}>= \varepsilon_0$. In (f), the polyhedra SKIZ is superimposed in blue.

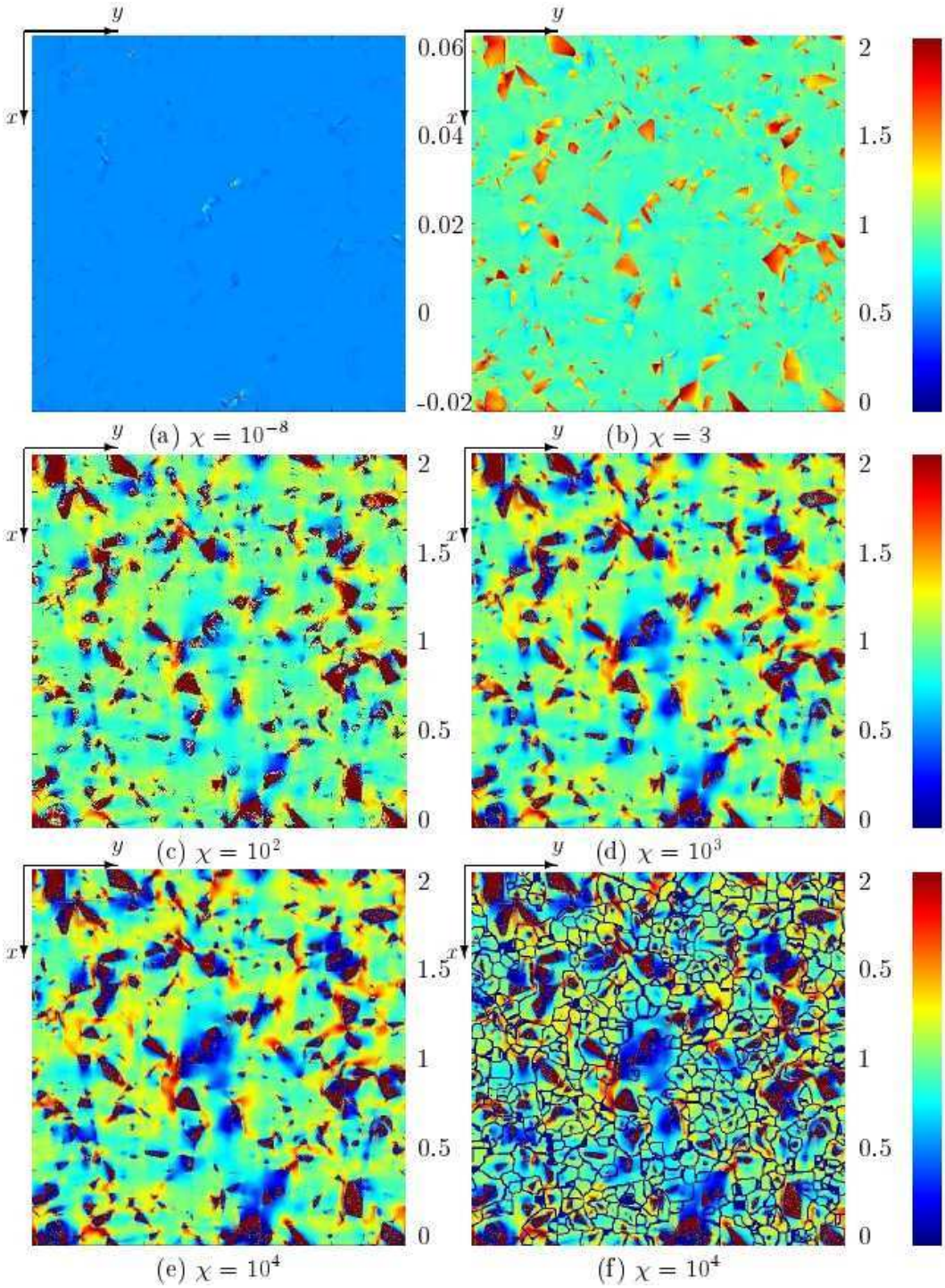


Fig. 21. 2D sections of the normalized stress component $\sigma_{xy}/[E^{(m)}<\varepsilon_{xy}>]$ at varying contrasts $\chi=E^{(a)}/E^{(m)}$. The field maps are thresholded according to the color-scale as shown right. Shear strain loading is applied with $<\varepsilon_{xy}>=\varepsilon_0$. In (f), the polyhedra SKIZ is superimposed in blue.

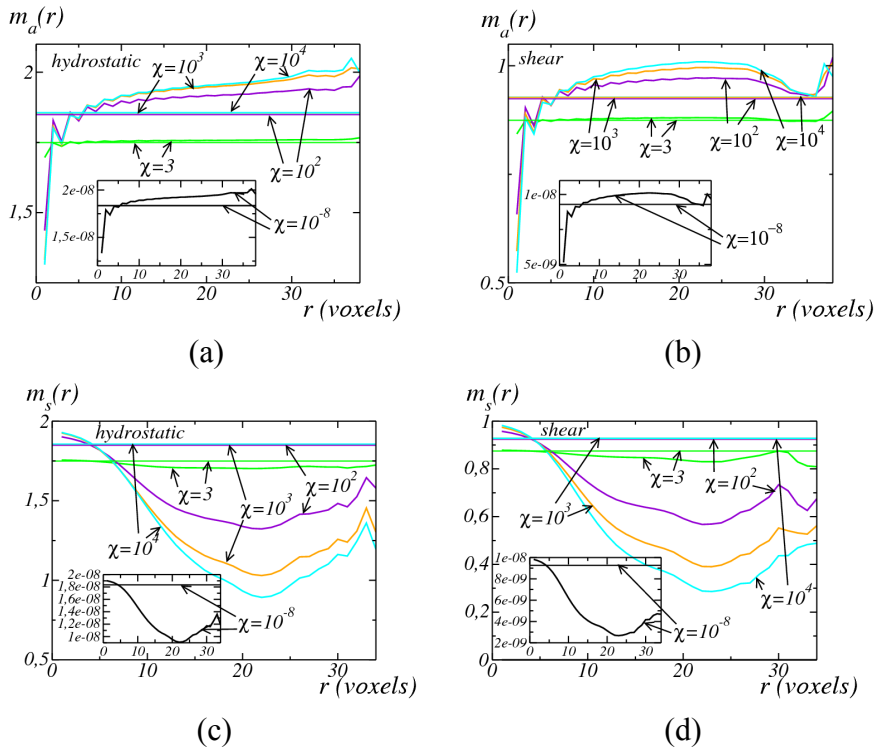


Fig. 22. Mean $m_{a,s}(r)$ of the parallel stress component σ_m or σ_{xy} as a function of the distance r at various aggregates/matrix contrasts χ. Fields are computed on a Boolean random Poison polyhedra realization. The distance r is computed from the aggregates (a, b) or from the aggregates SKIZ (c, d). Hydrostatic or shear strain loading is applied (a, c and b, d, resp.). A straight horizontal line indicates the mean stress component in the matrix, associated to each contrast value.

likewise for the highest principal stress and von Mises criterion. Moreover, the stress concentration on the SKIZ varies little with the distance between aggregates. In the hydrostatic mode, there is an additional concentration of the von Mises field at small distance of aggregates, whereas for the shear loading mode, local isotropic traction occurs at middle distance from aggregates. As for the transverse stress component (i.e. shear stress in the hydrostatic mode and vice-versa), regions of highest stress have been found both near the matrix/grains interface and along the SKIZ, however results are more difficult to interpret in this case. Higher stress area could be the location of damage initiation under load.

Finally, a preliminary microstructure model has been developed for mortar composites. It consists of a Boolean model of Poisson polyhedra. It shows a similar distribution of the fields in the matrix as the actual mortar. Such model may be easily generalized to multiscale Boolean models, where the size parameters are optimized with respect to the aggregates granulometry, and where the microstructure of simulations will be closer to the real microstructures, after identification of the model.

REFERENCES

Bary, B., Haha, M.B., Adam, E. and Montarnal, P. (2009), "Numerical and analytical effective elastic properties of degraded cement pastes". *Cement Concrete Res.*, Vol. **39**(10), 902-912.

Bentz, D. (1997), "Three-dimensional computer simulation of portland cement hydration and microstructure development". *J. Am. Ceram. Soc.*, Vol. **80**(1), 3-21.

Bernard, F., Kamali-Bernard, S. and Prince, W. (2008), "3d multi-scale modelling of mechanical behaviour of sound and leached mortar". *Cement Concrete Res.*, Vol. **38**(4), 449-458.

Escoda, J., Willot, F., Jeulin, D., Sanahuja, J. and Toulemonde, C. (2011), "Estimation of local stresses and elastic properties of a mortar sample by FFT computation of fields on a 3D image". *Cement Concrete Res.*, Vol. **41**(5), 542-556.

Haecker, C.J., Garboczi, E., Bullard, J., Bohn, R., Sun, Z., Shah, S. and Voigt, T. (2005), "Modeling the linear elastic properties of portland cement paste". *Cement Concrete Res.*, Vol. **35**(10), 1948-1960.

Hain, M. and Wriggers, P. (2007), "Numerical homogenization of hardened cement paste". *Comput. Mech.*, Vol. **42**(2), 197-212.

Granger, L. (1996), "Comportement différé du béton dans les enceintes de confinement de centrales nucléaires, analyse et modélisation d'ouvrage". Ph.D. thesis, Laboratoire Central des Ponts et Chaussées.

Jeulin, D. (1986), "Study of spatial distributions in multicomponent structures by image analysis", *Proceedings of the 4th European Symposium of Stereology*.

Lantuejoul, C. (1980), "Skeletonization in quantitative metallography", *Issues of Digital Image Processing*, Vol. **34**, 107-135.

Michel, J.C., Moulinec, H. and Suquet, P. (2001), "A computational scheme for linear and nonlinear composites with arbitrary phase contrast". *Int. J. Numer. Meth. Eng.*, Vol. **52**(1-2), 139-160.

Moulinec, H. and Suquet, P. (1994), "A fast numerical method for computing the linear and nonlinear mechanical properties of composites". *Comptes rendus de l'Académie des sciences. Série II*, Vol. **318**(11), 1417-1423.

Nagai, G., Yamada, T. and Wada, A. (1998), "Stress analysis of concrete material based on geometrically accurate finite element modeling". *FRAMCOS-3*.

Quenec'h, J.L., Coster, M., Chermant, J.L., and Jeulin, D. (1992) "Study of the liquid-phase sintering process by probabilistic models: application to the coarsening of WC-CO cermets". *J. Microsc.*, Vol**. 168**(1), 3-14.

Sanahuja, J. and Toulemonde, C. (2011), "Numerical homogenization of concrete microstructures without explicit meshes". *Cement Concrete Res.*, in press.

Serra, J. (1982), *Image Analysis and Mathematical Morphology*, Academic Press.

Šmilauer, V. and Bažant, Z. (2010), "Identification of viscoelastic c-s-h behavior in mature cement paste by fft-based homogenization method", *Cement Concrete Res.*, Vol. **40**(2), 197-207.